Available online at www.sciencedirect.com
ScienceDirect
Trans. Nonferrous Met. Soc. China 33(2023) 3427−3438
Transactions of Nonferrous Metals Society of China
www.tnmsc.cn

Effects of In addition on microstructure and properties of SAC305 solder

Xiao-lei REN, Yun-peng WANG, Yan-qing LAI, Shu-yan SHI, Xiao-ying LIU, Long-jiang ZOU, Ning ZHAO

School of Materials Science and Engineering, Dalian University of Technology, Dalian 116024, China

Received 30 March 2022; accepted 10 June 2022

Abstract: In powders with different contents (0.5−10 wt.%) were melted into the Sn−3.0Ag−0.5Cu (SAC305) solder to change the microstructure and thus improve the properties of the solder. The results showed that β-Sn(In), $Ag_3(Sn,In)$ and $Cu_6(Sn,In)_5$ phases existed in all the In-added solders, and an additional phase of $InSn_4$ was found in the SAC305−10In solder. With increasing In addition amount, the β-Sn nucleation sites were increased and the nucleation model was changed from {101} to {301}, which refined the β-Sn grains and transformed the β-Sn morphology from large grains to interlaced grains and finally to multiple grains. As a result, a combined effect of fine grain strengthening and solid solution strengthening was achieved to increase the microhardness of the SAC305−xIn solders with increasing In addition amount.

Key words: Sn−3.0Ag−0.5Cu; In; β-Sn; undercooling; nucleation model; microhardness

1 Introduction

With rapid development of electronic components, the development of soldering techniques in microelectronic assembly and packaging has put forward increasing requirements [1,2]. Sn−Ag−Cu (SAC) solder alloys are most widely used so far because of their excellent mechanical properties and wettability. Although the application scenarios of SAC solder alloys are extremely extensive, there are still some problems to be solved, such as coarse β-Sn grains. Previous study reported that only a few of β-Sn grains existed in SAC305/Cu solder joints, while the size of β-Sn grains in SAC305 ingots could be as large as 3000 μm [3−6]. For electronic packaging, the orientation of β-Sn grains is not only closely related to mechanical properties but also seriously affects the thermophysical properties and electromigration lifetime of solder joints. Therefore, it is necessary to control the grain size of β-Sn to improve the overall performance of solder joints.

A large body of methods have been explored to refine the β-Sn grains in solders, i.e., ultrasonic treatment [7−9], cooling rate control [10,11] and dilute element addition [4,6,12,13]. Generally, controlling process conditions have little effect on the microstructure of solders and are difficult to operate in a real reflow. However, the method of element addition can improve the microstructure of solder alloys, so some alloying elements have been added to solder materials, such as Ni [14−17], Sb [18], Co [4], Zn [19,20], Bi [21], and rare-earth elements [22]. SEO et al [23] revealed that minor alloying addition of Ni or Zn to Sn−Ag solder led to the microstructure coarsening drastically and the undercooling decreasing. HAN et al [24] reported that the grain size of SAC solder alloys with Ag−GNSs addition was lower than that of SAC and the mechanical properties of SAC solder alloys with 0.2Ag−GNSs particles were greatly improved.

Recently, In has been drawn attention as an alloying element to improve the performance of lead-free solders. CHEN et al [25] reported that with In addition the elongation and tensile strength

Corresponding author: Ning ZHAO, Tel: +86-18342237603, E-mail: zhaoning@dlut.edu.cn
DOI: 10.1016/S1003-6326(23)66344-7

of Sn−58Bi increased slightly. TIAN et al [26] reported that doping In into Sn−0.7Cu solder could improve not only the maximum bending properties of solder joints but also the aging performance. TIAN et al [27] found that the UTS of Sn−0.7Cu−*x*In alloys increased obviously but meanwhile the elongation decreased significantly. Moreover, when the In content increased to 1.0 wt.%, coarse $Cu_6(Sn,In)_5$ IMC were formed in the solder alloy. Despite the fact that some studies have been conducted on solder alloys with In addition, few studies have focused on the effect of In addition on β-Sn grain size of solder alloys.

In this study, the effects of In addition on the thermodynamic characteristics, microstructures and mechanical properties of SAC305 solder were investigated. To characterize β-Sn grain size more accurately, SAC305−*x*In solder sheets were used because of their larger size than solder joints.

2 Experimental

The SAC305−*x*In (*x*=0, 0.5, 1, 2, 5, 10 wt.%) solders were prepared by using SAC305 solder paste and In powders. The SAC305 solder paste mainly consisted of 88.5 wt.% SAC305 alloy powders and 11.5 wt.% flux and was made by Alpha Technologies. The In powders were made by Xiangtian Nano Co., Ltd. The SAC305 solder paste and the In powders were mixed together according to the designed composition ratios by mechanical stirring to form SAC305−*x*In composite solder paste. Then, the SAC305−*x*In composite paste (3 g) were printed between two ceramic plates and reflowed using a hot plate at 250 °C with a duration of 2 min. Hereafter, the samples were cooled down with the hot plate under a cooling rate of about 6 °C/min until solidification. Finally, SAC305−*x*In solder sheets were obtained and cleaned with alcohol.

For thermal behavior analysis, samples of about 1 mg were taken from each kind of the solder sheets. Then, the samples were measured by a differential scanning calorimeter (DSC, Mettler-Toledo 822) in argon atmosphere. The samples were firstly heated up at a rate of 5 K/min to the peak temperature of 250 °C, held for 30 s and then cooled down at 5 K/min. For phase analysis, the solder sheets were examined by using X-ray diffraction (XRD, Empyrean). For microstructure and phase composition characterization, some of the solder sheets were mounted in resign following by grinding and polishing. Hereafter, the polished solder sheets were etched by using a solution of 92% CH_3OH + 5% HNO_3 + 3% HCl (vol.%) for 2 min. And then, the microstructure including β-Sn grain feature and phase composition of all the solders were examined by a scanning electron microscope (SEM, Zeiss SUPRA55) equipped with an electron backscattered diffraction (EBSD, NordlysMax2) and an electron probe micro analyzer (EPMA, JEOL JXA8500F). In addition, Vickers hardness (HV) test was applied to the polished solder sheets under a load of 50 g and a duration of 15 s for mechanical property analysis.

3 Results

3.1 Thermodynamic property of SAC305−*x*In solders

Figure 1 shows the DSC curves of the SAC305−*x*In solders. In order to simplify the DSC curves, only the fragments of the endothermic and exothermic peaks were chosen, which is different from the traditional DSC curves. Moreover, the melting range and undercooling of these solders were calculated, as listed in Table 1. The melting range obtained from each DSC curve was defined as the temperature difference between the onset melting temperature ($T_{onset\text{-}H}$) and the endset melting temperature ($T_{endset\text{-}H}$) during the heating process. The melting range of a solder alloy is closely related to oxide slag defects during solidification and will seriously affect the reliability of solder joints. In addition, the undercooling, ΔT, was defined as the temperature difference between the

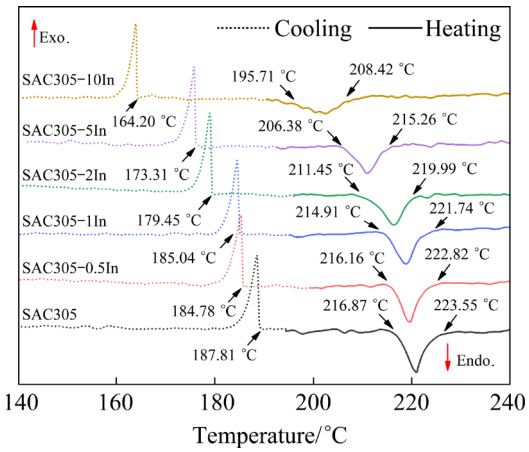

Fig. 1 DSC curves of SAC305−*x*In solders

Table 1 Thermodynamic properties of SAC305−*x*In solders

Solder	$T_{onset-H}$/°C	$T_{endset-H}$/°C	$T_{onset-C}$/°C	Melting range/°C	ΔT/°C
SAC305	216.87	223.55	187.81	6.68	29.06
SAC305−0.5In	216.16	222.82	184.78	6.66	31.38
SAC305−1In	214.91	221.74	185.04	6.83	29.87
SAC305−2In	211.45	219.99	179.45	8.54	32.00
SAC305−5In	206.38	215.26	173.31	8.88	33.07
SAC305−10In	195.71	208.42	164.20	12.71	31.51

$T_{onset-H}$ during heating and the onset solidification temperature ($T_{onset-C}$) during cooling. Generally, ΔT is closely related to the nucleation and growth rate of grains and will directly affect the microstructure of the solidified alloy.

During heating as shown in Fig. 1, with the increase of In content, the melting point, i.e., $T_{onset-H}$, of SAC305−*x*In solders was gradually decreased and the decreasing trend remained virtually unchanged; while the melting range showed an increasing trend with the increase of In addition, especially at and after 2 wt.% In. Combining with the data in Table 1, when the In addition was less than 2 wt.%, the melting range was basically fluctuated around 6.7 °C; when the In addition increased from 2 to 5 wt.%, the melting range increased slowly to 8.88 °C with an increment of only 2.2 °C compared to the SAC305 solder; however, when the In addition was larger than 5 wt.%, the melting range increased significantly to 12.71 °C. Although the melting range is closely related to the melting point, the change of the melting point was not consistent with the change of melting range for SAC305−*x*In solders. Moreover, the undercooling, ΔT, was slightly increased by In addition with a maximum increment of about 4 °C, which could have effect on the nucleation rate of the solders to some extent.

3.2 Phase composition and element distribution of SAC305−*x*In solders

Figure 2 shows the XRD patterns of the SAC305−*x*In solders. It can be found that the peaks of the *β*-Sn, Ag_3Sn and Cu_6Sn_5 phases were detected on all the XRD patterns. Besides, with the In addition of 5 wt.%, a small peak of Ag_2In phase appeared on the XRD pattern. As the addition of In reached 10 wt.%, the peaks of both Ag_2In and $InSn_4$ phases were found on the XRD patterns, but it seemed that the peak intensity of Ag_3Sn and Cu_6Sn was much lower than that for other SAC305−*x*In (*x*=0, 1, 2, 5 wt.%) solders. This indicates that when the In content increased to 10 wt.%, In atoms mainly formed Ag_2In and $InSn_4$ IMCs besides dissolving into the Sn matrix. In addition, it is deduced that when the In content was less than or equaled to 2 wt.%, In atoms should be dissolved in the *β*-Sn, Ag_3Sn and Cu_6Sn_5 phases without changing their crystal structure. *β*-Sn, Ag_3Sn and Cu_6Sn_5 are common phases in the Sn−Ag−Cu phase diagram, as shown in Fig. S1 (Supplementary Information, SI). According to the phase distribution in the Sn−Ag−In phase diagram shown in Fig. S2 (see SI), it can be found that Ag_2In and $InSn_4$ would form with the increase of In content. Combined with the XRD results, the evolution of phases in the solders basically agreed well with the phase diagrams.

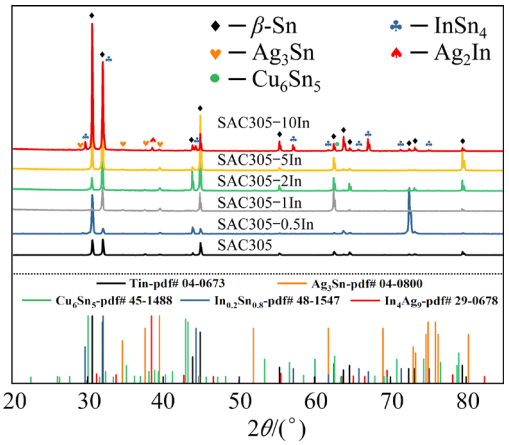

Fig. 2 XRD patterns of SAC305−*x*In solders

Figure 3 shows the backscattered electron (BSE) images of the SAC305−*x*In solders. The corresponding composition analysis results of the precipitated phases at different positions and the solder matrix at different regions in Fig. 3 are listed in Tables 2 and 3, respectively. According to Fig. 3(a), the SAC305 solder showed a typical microstructure consisting of the *β*-Sn (grey regions) primary phase and the light and dark precipitated phases. From the composition results at Positions 1 and 2, it can be known that the light and dark precipitated phases were Ag_3Sn and Cu_6Sn_5, respectively. The XRD pattern analysis shows that the above three phases were also presented in the SAC305−*x*In solders. Combining the composition analysis data in Tables 2 and 3, the content of In in

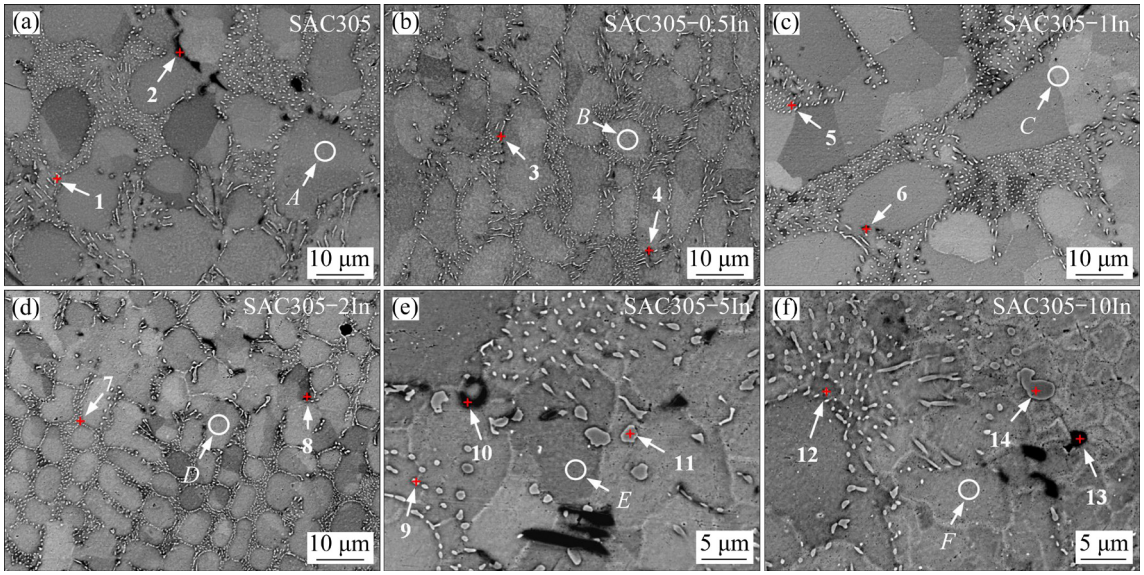

Fig. 3 BSE images of SAC305−*x*In solders: (a) *x*=0; (b) *x*=0.5; (c) *x*=1; (d) *x*=2; (e) *x*=5; (f) *x*=10

Table 2 Element contents of precipitated phases at different positions in Fig. 3 (at.%)

Position	Sn	Ag	Cu	In
1	36.7	62.9	0.4	–
2	51.4	0.5	48.1	–
3	40	58.1	1.9	–
4	46.8	0.9	52.3	–
5	34.5	65	0.5	–
6	49	0.4	50.6	–
7	29.7	62.9	0.3	7
8	44.9	0.5	53.5	1.1
9	28.4	68.8	0.2	2.4
10	43.4	0.4	53.9	6.7
11	6.4	75	0.3	18.3
12	13.5	77	0.5	9
13	40	0.4	53.9	6.7
14	3.2	63.5	0.1	22.2

Table 3 Element contents of solder matrix at different regions in Fig. 3 (at.%)

Region	Sn	Ag	Cu	In
A	99.9	0.1	–	–
B	99.8	–	0.2	–
C	99.7	0.1	0.2	–
D	98.7	1.2	–	–
E	99.1	0.3	0.2	0.4
F	97.3	–	–	2.5

the $Ag_3(Sn,In)$, $Cu_6(Sn,In)_5$ and β-Sn generally increased with the increase of In addition, since In mainly existed as solid solution atoms in these phases before the formation of Ag_2In and $InSn_4$ IMCs. However, the increase of In content in the $Ag_3(Sn,In)$ was significantly faster than those in $Cu_6(Sn,In)_5$ and β-Sn, indicating that In was more stable in $Ag_3(Sn,In)$ than in the other two phases. Moreover, combining the composition analysis data at the Positions 11 and 14 and the XRD data, the grey bulk precipitated phase that contained more In than the grey fine $Ag_3(Sn,In)$ particles should be $Ag_2(In,Sn)$ phase. This was further confirmed in Figs. S3 and S4 (see SI).

It should be noted that the $InSn_4$ phase was not observed in the BSE images in Fig. 3, which is inconsistent with the XRD results. In addition, more evidence should be presented to prove that In was dissolved in the Ag_3Sn and Cu_6Sn_5 phases. Therefore, additional testing method is required to examine the distribution of these phases. Figure 4 shows the microstructure and element mappings of the SAC305−*x*In solders. As shown in Figs. 4(b) and (g), the crystal structure of the Ag_3Sn and Cu_6Sn_5 phases were determined by EBSD analysis and In element was detected in both phases. In addition, the In brightness at the $Ag_3(Sn,In)$, $Cu_6(Sn,In)_5$ and β-Sn positions in Fig. 4(g) gradually increased with the increase of In addition. Therefore, it can be concluded that the Ag_3Sn and Cu_6Sn_5 phases were gradually transformed into $Ag_3(Sn,In)$ and $Cu_6(Sn,In)_5$ due to the dissolution of

In. When the In addition was as low as 0.5 wt.%, In element uniformly distributed in the β-Sn matrix. According to the element distribution of Ag, Cu and In, it is obvious that the In element trended to aggregate at where the Ag element distributed with the In addition being or being higher than 1 wt.%. This further verified that In was more stable in the $Ag_3(Sn,In)$ than in the $Cu_6(Sn,In)_5$ and β-Sn. When the In addition increased to 10 wt.%, the regions of In aggregation were detected as circled by the white dashed line in Fig. 4(g_5), which was consistent with the position of $InSn_4$ in Fig. 4(b_5). Thus, $InSn_4$ phase formed in the SAC305−10In solder. Furthermore, no $InSn_4$ phase was detected when the In content was below 10 wt.%, which was consistent with the XRD results.

3.3 Effect of In addition on phase morphology of SAC305−*x*In solders

Figure 5 shows the BSE images and the corrosion morphologies of the SAC305−*x*In solders. According to the BSE images, the Cu_6Sn_5 and $Cu_6(Sn,In)_5$ phases in the form of dots or short rods were randomly distributed in the SAC305−*x*In solders and did not vary with the increasing In content. However, the β-Sn and $Ag_3(Sn,In)$ phases

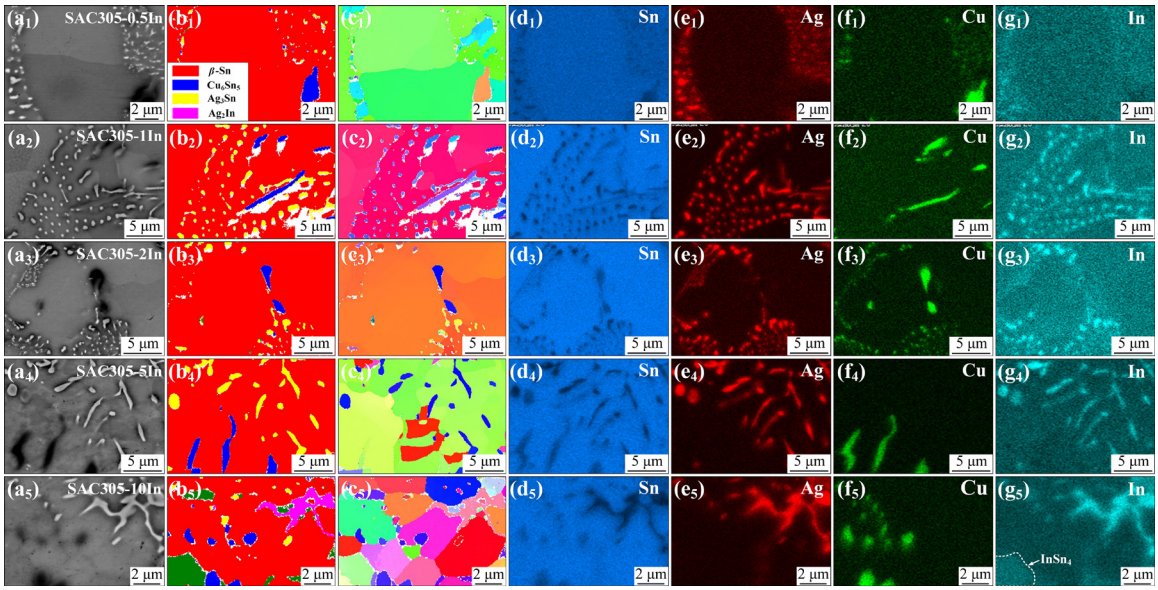

Fig. 4 Microstructures and element mappings of SAC305−*x*In solders: (a) BSE maps; (b) Phase distribution maps; (c) IPF-X maps; (d−g) Sn, Ag, Cu and In element distribution maps, respectively

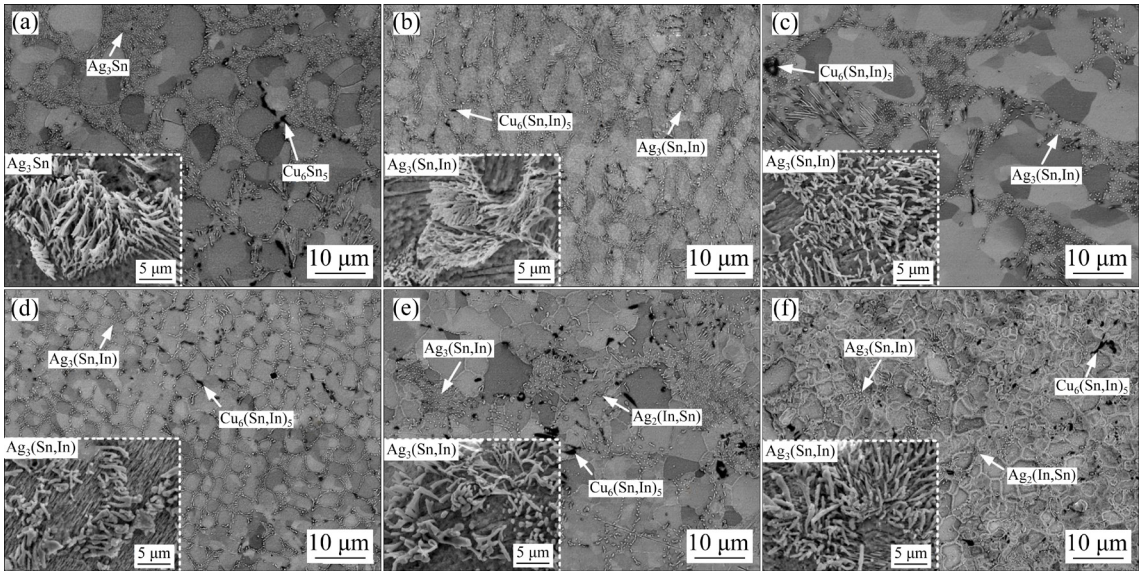

Fig. 5 BSE images and corrosion morphologies of SAC305−*x*In solders: (a) *x*=0; (b) *x*=0.5; (c) *x*=1; (d) *x*=2; (e) *x*=5; (f) *x*=10

showed different morphologies in different solders. When a small amount of In was added, β-Sn was relatively flat which was similar to the SA305 solder. As the In addition increased, β-Sn was severely deformed, which may be because of the strong deformation caused by the solid solution of In into β-Sn. However, only a little information could be captured from the BSE images, so this will be discussed in detail with EBSD characterization later.

The morphology change of Ag_3Sn and $Ag_3(Sn,In)$ phases could be clearly observed from the corrosion morphology at the lower left corner of each BSE image. As shown in Figs. 5(a, b), it can be found that the Ag_3Sn in the SAC305 solder and the $Ag_3(Sn,In)$ in the SAC305−0.5In solder were all needle-like and smaller than 1 μm in width. As shown in Figs. 5(c−f), though the morphology of $Ag_3(Sn,In)$ phase was still needle-like, it gradually coarsened with increasing In content, which is similar to the previous study [28]. It has been reported that Ag_3Sn is precipitated in eutectic form in the SAC305 solder and the short growth time leads to the fine needle-like morphology [29]. However, with the increase of In content, $Ag_3(Sn,In)$ had a longer time to grow due to the larger undercooling, which led to the coarsening of the $Ag_3(Sn,In)$ phase.

3.4 Effect of In addition on β-Sn grain feature of SAC305−*x*In solders

Figure 6 shows the IPF-X orientation maps and the corresponding {001} pole figures of the SAC305−*x*In solders. It can be seen from Fig. 6(a) that there were only two β-Sn grains in the SAC305 solder, i.e., the green one and the striped pink one. With a small amount of In addition of 0.5 wt.%, a strong preferred orientation was observed, indicating that the SAC305−0.5In solder nearly consisted of single oriented grain with some sub-boundaries inside. As the In addition increased, the number of β-Sn grains increased gradually. When the In addition increased to 5 wt.%, the resultant β-Sn grains were much more than those in the SAC305−1In and SAC305−2In solders. Nevertheless, as shown in Fig. 6(e), only five intensive points were presented, indicating that there was still a few β-Sn grains. As the In addition reached 10 wt.%, the morphology of β-Sn transformed into multiple grains with an average grain size less than 5 μm. Although multiple grains presented in the SAC305−10In solder, the {001} pole figure in Fig. 6(f) indicates that the β-Sn grains still had preferred orientation.

Figure 7 shows the grain boundary angle misorientation mappings of the SAC305−*x*In solders shown in Fig. 6. It can be seen that the mappings contained three kinds of colored lines, i.e., red, green and black, which presented the grain boundary angles less than 15°, in the range of 57°−63° and more than 63°, respectively. It was previously reported that the twin boundary angles in Sn-based solder alloys were always 57.2° or 62.8°, respectively [30]. Thus, the red, green and black lines actually presented low-angle, twin and large-angle boundaries, respectively. By matching

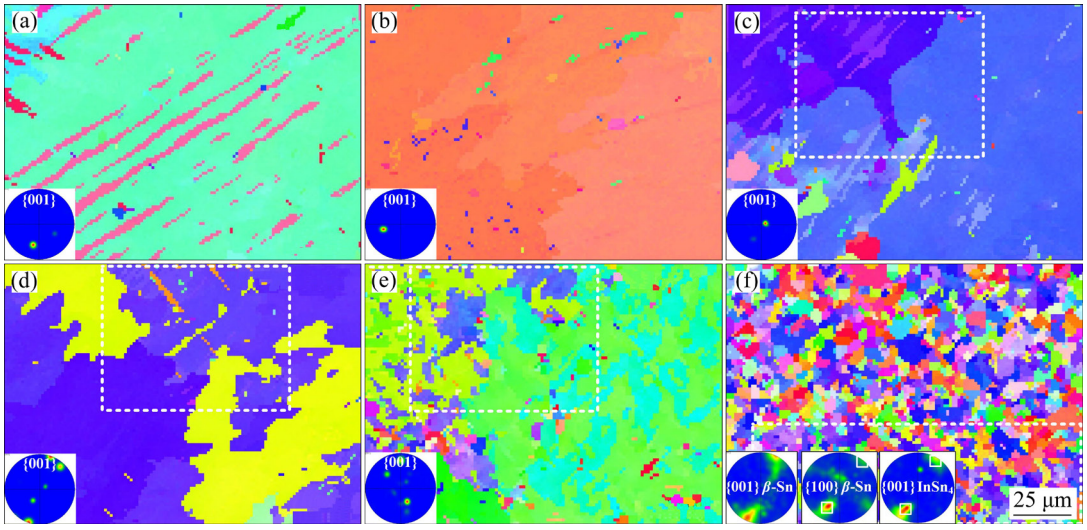

Fig. 6 IPF-X orientation maps and corresponding {001} pole figures of SAC305−*x*In solders: (a) *x*=0; (b) *x*=0.5; (c) *x*=1; (d) *x*=2; (e) *x*=5; (f) *x*=10

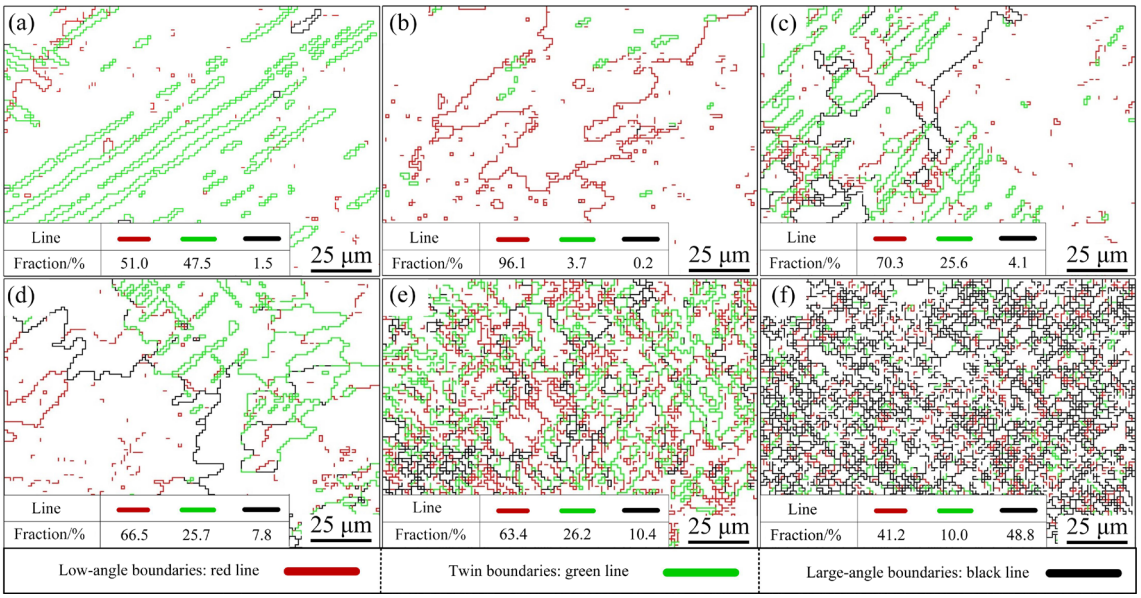

Fig. 7 Grain boundary angle misorientation mappings of SAC305−*x*In solders in Fig. 6: (a) *x*=0; (b) *x*=0.5; (c) *x*=1; (d) *x*=2; (e) *x*=5; (f) *x*=10

Figs. 6 and 7, it was found that there were almost the low-angle and twin boundaries in the SAC305 and SAC305−0.5In solders. Therefore, it could be concluded that the grains in Figs. 6(a, b) formed from only one nucleation site. As the In addition increased, it was found that the low-angle and twin boundaries decreased, while the large-angle boundary increased, indicating that In played an important role in refining *β*-Sn grains. It is worth noting that although In had a significant effect on the refinement of the solders, but twinned grains in the high In content solder also existed, i.e, SAC305−10In. Therefore, the growth pattern of the *β*-Sn grains in the SAC305−*x*In solders needs to be further discussed.

3.5 Microhardness of SAC305−*x*In solders

Figure 8 shows the microhardness of the SAC305−*x*In solders. On the whole, the microhardness increased gradually with increasing In addition. According to the previous study that In could dissolve into *β*-Sn to produce solid solution strengthening [27], the In-bearing solders should be harder than the SAC305 solder. In addition, it was found in Section 3.4 that the addition of In could refine the *β*-Sn grains. The relationship between the microhardness (H_v) and the grain size (d) can be established in relation with the derived Hall−Petch formula [31]:

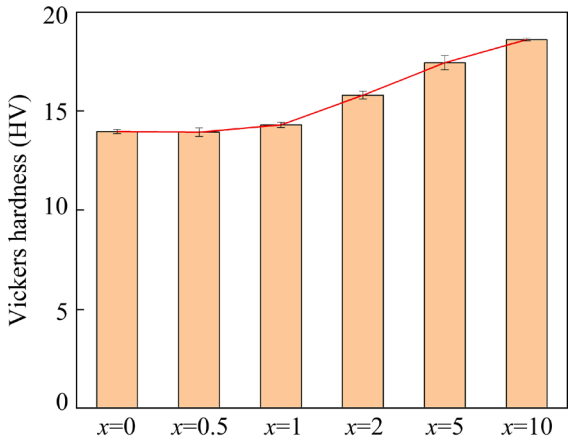

Fig. 8 Variation of microhardness with In content of SAC305−*x*In solders

$$H_v = H_{v_0} + K_H d^{-1/2} \quad (1)$$

where H_{v0} is the hardness of the single crystals, and K_H is a material constant.

According to Eq. (1), it can be concluded that the refinement of *β*-Sn grain by In addition also played an important role in the increase of microhardness. When a small amount of In (≤1 wt.%) was added, the microhardness increased slightly. This indicated that adding a small amount of In had little effect on the mechanical property of the SAC305 solder. When the In addition was larger than 1 wt.%, the microhardness increased significantly and presented a linearly increasing

trend up to 10 wt.%. As previously mentioned, In mainly existed in the form of $Ag_3(Sn,In)$, so its effect on the microstructure and mechanical property of the solders was limited. As the In addition further increased, In could not only dissolve into the β-Sn grains to generate solid solution strengthening but also refine the β-Sn grains to generate fine grain strengthening. As a result, the microhardness of the solders increased significantly.

4 Discussion

4.1 Effect of In addition on β-Sn growth pattern of SAC305−xIn solders

According to the above results, β-Sn grain size was closely related to the In content in the solders and the number of β-Sn grains can significantly affect the properties of solder joints. In order to further improve the microstructure of the solders, it is necessary to explore the mechanism of the effect of In addition on β-Sn grain size. LEHMAN et al [30] reported that two morphologies of β-Sn grains with twin orientation were observed in SAC305 solder, i.e., beach ball morphology and interlaced grain morphology, which were nucleated and grew with the {101} and {301} nucleus models, respectively. Accordingly, the {101} and {301} nucleation models were exhibited in Figs. 9(a−d) and Figs. 9(e, f), respectively. The {101} nucleus model is a hexagonal-bipyramidal dodecahedron and the surfaces are all (110) planes (triangular shape). When the solder was nucleated with the {101} nucleus model and the β-Sn dendrites grow along the [110] direction, beach ball morphology will be formed. The surface of the {301} nucleus model also contains many (110) planes, but its shape is much different from the {101} nucleus model. When the β-Sn dendrites of solders were nucleated with {301} nucleus model and grow along the [110] direction, interlaced grain morphology will be formed.

It is worth noting that the beach ball morphology contained three large β-Sn twin grains that were much larger than those with the interlaced grain morphology. As previous study reported that the growth rate of Sn dendrites could reach ~40 cm/s in Sn-based solder alloys [32]. Thus, if the solder alloy solidified with the {101} nucleation model, large twinned β-Sn grains would form quickly, because β-Sn dendrites could grow rapidly before the other nucleation sites form around in the molten solder. Therefore, combined the β-Sn grain feature shown in Fig. 6, it can be concluded that the SAC305−xIn (x=0, 0.5, 1, 2 wt.%) and SAC305−xIn (x=5, 10 wt.%) solders nucleated and grew following the {101} and {301} nucleus models, respectively.

According to the findings of β-Sn grains and the nucleation site of the SAC305 and SAC305−0.5In solders in Section 3.4, it can be deduced that the β-Sn grains were nucleated and grew based only one {101} nucleation model, as illustrated in Figs. 9(a, b). Figure 10 shows the partially zoom

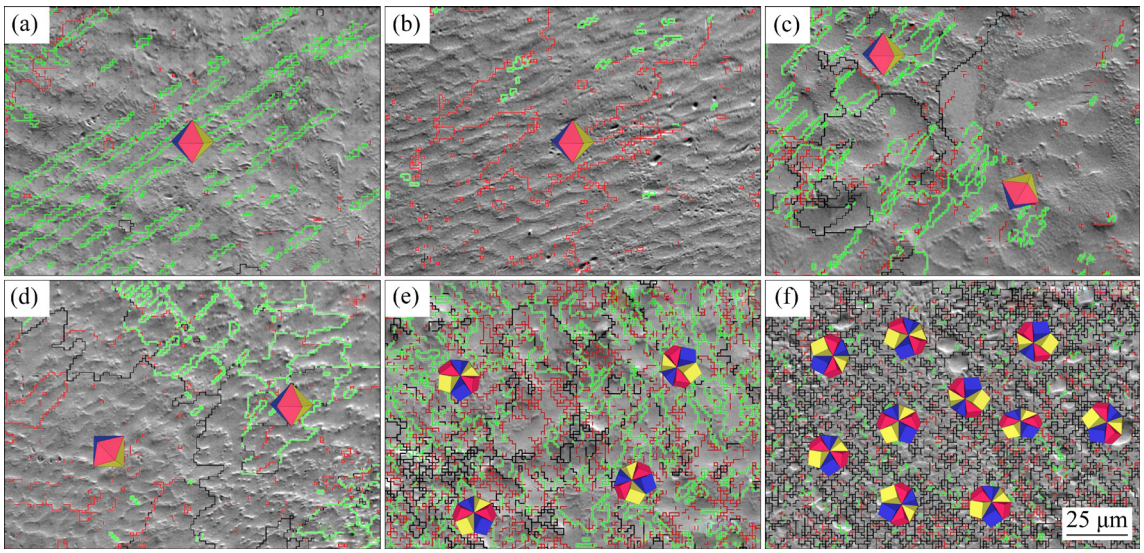

Fig. 9 Relationship between nucleation model and microstructure of SAC305−xIn solders: (a) x=0; (b) x=0.5; (c) x=1; (d) x=2; (e) x=5; (f) x=10

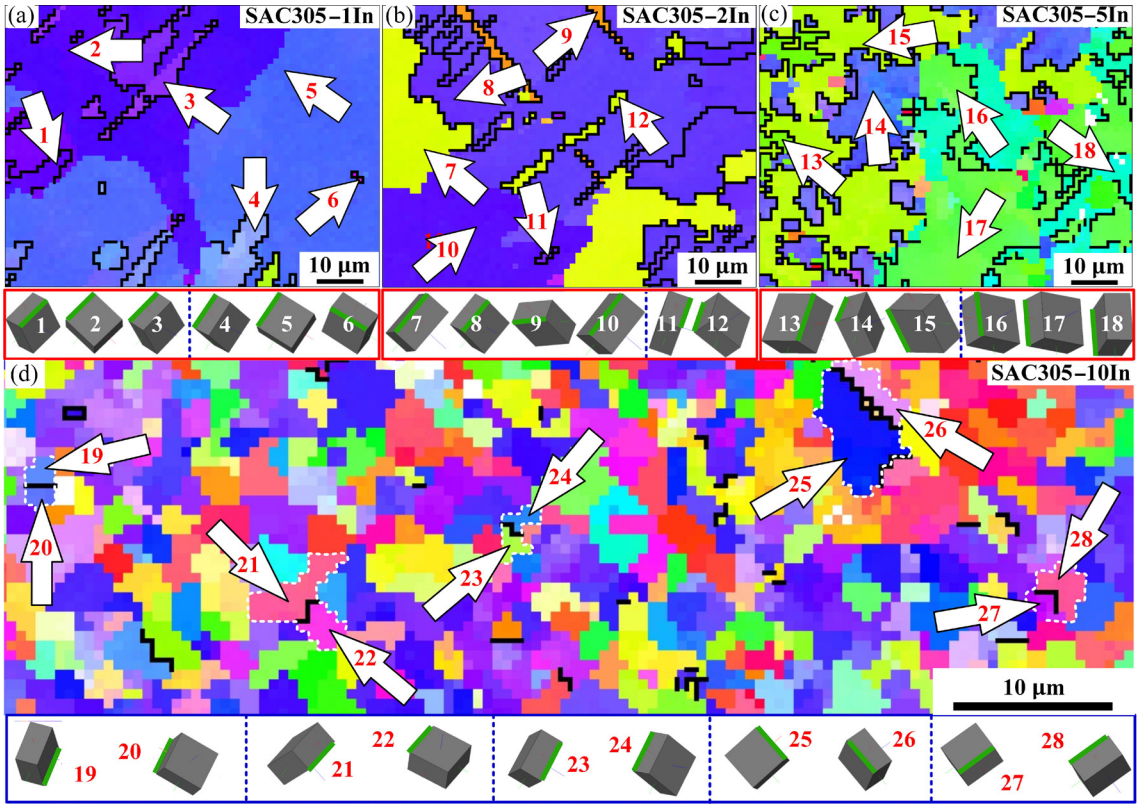

Fig. 10 Partially zoom view of IPF-X maps (a−d) corresponding Figs. 6(c−f), respectively

view of the *β*-Sn grains inside the white dashed boxes in Fig. 6, where the black lines represent twin grain boundary. As shown in Fig. 10(a), the six unit cells presented the different orientations, where unit cells 1, 2 and 3 and cells 4, 5 and 6 had a twin orientation relationship, respectively. However, there was no orientation relationship between these two groups of the unit cells. Thus, it can be concluded that two {101} nucleation models existed in this region, as illustrated in Fig. 9(c). Similar phenomena were also detected in the SAC305−2In solder as shown in Fig. 10(b).

With the In addition increasing to 5 wt.%, the morphology of the *β*-Sn grains changed from large grain to interlaced grain, but still exhibited a strong twinning relationship as shown in Fig. 10(c). The orientations of the twinned unit cells 1, 2 and 3 were completely different from those of the twinned unit cells 4, 5 and 6 on the other side of the large angle grain boundary. Combining the *β*-Sn morphology and grain boundary of the SAC305−5In solder, there must be several {301} nucleation models in this region, as illustrated in Fig. 9(e). As the In addition increased to 10 wt.%, multiple *β*-Sn grain morphologies were presented, but a large number of the *β*-Sn grains remained the twinning relationship. As shown in Fig. 10(d), four groups of the *β*-Sn unit cells with twinning relationship were displayed. These four groups had no orientation relationship with each other, suggesting that multiple twin nucleation models existed in the SAC305−10In solder, as illustrated in Fig. 9(f). When the amount of In increased, the lattice of the *β*-Sn cell was distorted [33], and thus the growth rate of *β*-Sn dendrites may be decreased, leading to an increase in nucleation site. Therefore, the morphology of the SAC305−10In solder presented as multiple grains mixed with twin grains.

4.2 Orientation relationship between *β*-Sn and $InSn_4$ compound

Figure 11 shows the orientation relationship (OR) between the *β*-Sn and $InSn_4$ phases in the SAC305−10In solder. According to the pole figures of the two positions in the SAC305−10In solder, the preference in the $\{100\}_{\beta\text{-Sn}}$ pole figure consisted with that in the $\{001\}_{InSn_4}$ pole figure. Therefore, it can be concluded that the OR between *β*-Sn and

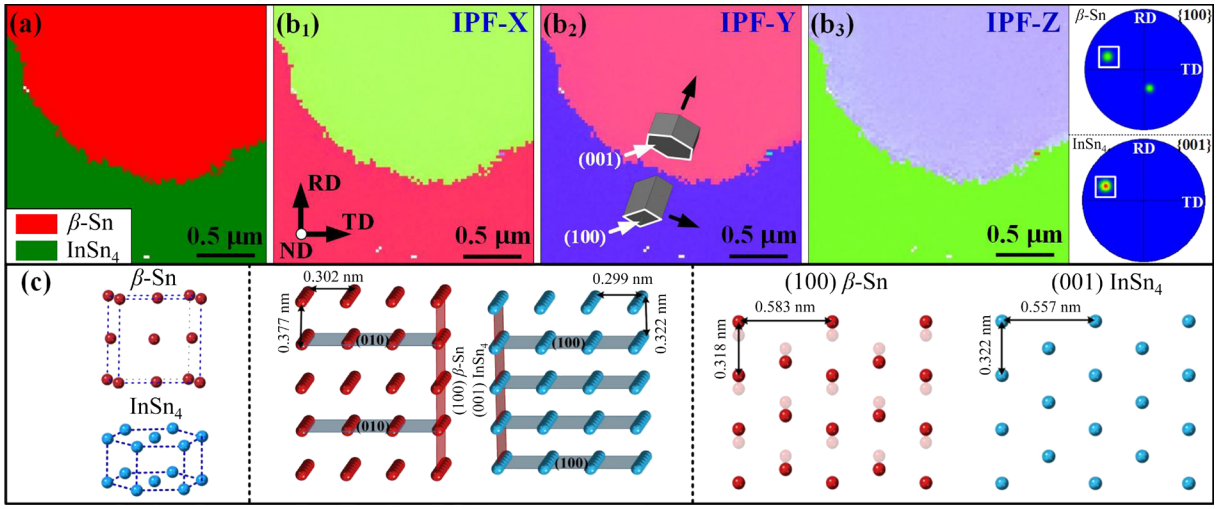

Fig. 11 Orientation relationship between β-Sn and $InSn_4$ phases in SAC305−10In solder: (a) Phase distribution maps; (b) IPF orientation maps; (c) Lattice matching relationship

$InSn_4$ could be exhibited as follows: $\{100\}_{\beta\text{-Sn}}$// $\{001\}_{InSn_4}$ and $[001]_{\beta\text{-Sn}}$//$[010]_{InSn_4}$. The fixed common direction $[001]_{\beta\text{-Sn}}$//$[010]_{InSn_4}$ but variable common plane can be understood by examining the β-Sn and $InSn_4$ atomic lattice match in Fig. 11(c). When the $(010)_{\beta\text{-Sn}}$ plane meets the $(100)_{InSn_4}$ plane with the $[001]_{\beta\text{-Sn}}$ direction parallel to the $[010]_{InSn_4}$ direction, the $(100)_{\beta\text{-Sn}}$ and $(001)_{InSn_4}$ planes exhibit a small d-spacing mismatch (<15%).

According to the {100} pole figure of β-Sn and {001} pole figure of $InSn_4$ in Fig. 6(f), the strong preference in the $\{100\}_{\beta\text{-Sn}}$ pole figure consisted with that in the $\{001\}_{InSn4}$ pole figure. As previous study reported, $InSn_4$ solidified preferentially over β-Sn in Sn−xAg−xIn solder [34]. Combining the orientation relationship between β-Sn and $InSn_4$, it can be deduced that the preferential orientation of the β-Sn grains in the SAC305−10In solder was caused by the influence of the $InSn_4$ phase. During the cooling process, the surface of the solders would cool down first, and the a temperature gradient (parallel to ND) could be developed from inside the solder towards the surface. As previous studies reported that temperature gradient was closely related to the orientation of solidified phases [35−37], so the preferred orientation of $InSn_4$ could be caused by the temperature gradient. The mechanism for producing such preferred grains could be similar to that in directional solidification. A comprehensive experiment to verify this preliminary assumption is in progress.

5 Conclusions

(1) The melting point, $T_{onset\text{-}H}$, of the SAC305−xIn solders decreased gradually with increasing In addition. The nucleation undercooling, ΔT, was slightly increased within 4 °C by all In additions.

(2) With the In addition into the SAC305 solder, the β-Sn, Ag_3Sn and Cu_6Sn_5 transformed to β-Sn(In), Ag_3(Sn,In) and Cu_6(Sn,In)$_5$, respectively. Moreover, a new phase of Ag_2(In,Sn) was found in the SAC305−5In solder, while a new phase of $InSn_4$ was found in the SAC305−10In solder besides Ag_2(In,Sn).

(3) Large size β-Sn grains were derived from the {101} nucleation model in the SAC305−xIn (x= 0, 0.5, 1, 2 wt.%) solders. As the In addition increased to 5 wt.%, smaller and more β-Sn grains were derived from the {301} nucleation model, showing an interlaced grain morphology. Hereafter, as the In addition further increased to 10 wt.%, the β-Sn grains were significantly refined, showing a multiple grain morphology with the existence of a large amount of twin grains.

(4) The hardness of the SAC305−xIn solders increased with increasing In content because of the coupling effect of fine grain strengthening and solid solution strengthening caused by In element.

Acknowledgments

This work was supported by the National Natural Science Foundation of China (No. 52075072).

Supplementary Information

Supplementary Information in this paper can be found at: http://tnmsc.csu.edu.cn/download/15-p3427-2022-0372-Supplementary_Information.pdf.

References

[1] HUMPSTON G, JACOBSON D M. Principles of soldering [M]. Materials Park, Ohio: ASM International, 2004.

[2] SERAPHIM D P, LASKY R, LI C Y, ENGEL P A. Principles of electronic packaging [J]. Journal of Electronic Packaging, 1989, 111(2): 162−163.

[3] QIAO Y Y, LIU X Y, MA H T, ZHAO N. Strategies for inducing heredity of β-Sn texture in micro solder joints during multi-reflow process [J]. Materials and Design, 2021, 204: 109671.

[4] MA Z L, BELYAKOV S A, GOURLAY C M. Effects of cobalt on the nucleation and grain refinement of Sn−3Ag−0.5Cu solders [J]. Journal of Alloys and Compounds, 2016, 682: 326−337.

[5] REN X L, WANG Y P, LIU X Y, ZOU L J, ZHAO N. Process dependence and nucleus models of β-Sn grains in SAC305 freestanding solder balls and BGA solder joints [J]. Journal of Materials Processing Technology, 2022, 302: 117468.

[6] SHANG H, MA Z L, BELYAKOV S A, GOURLAY C M. Grain refinement of electronic solders: The potential of combining solute with nucleant particles [J]. Journal of Alloys and Compounds, 2017, 715: 471−485.

[7] HU X W, XU H, CHEN W J, JIANG X X. Effects of ultrasonic treatment on mechanical properties and microstructure evolution of the Cu/SAC305 solder joints [J]. Journal of Manufacturing Processes, 2021, 64: 648−654.

[8] JI H J, WANG Q, LI M Y, WANG C Q. Effects of ultrasonic irradiation and cooling rate on the solidification microstructure of Sn−3.0Ag−0.5Cu alloy [J]. Journal of Materials Processing Technology, 2014, 214: 13−20.

[9] JI H J, WANG Q, LI M Y, WANG C Q. Ultrafine-grain and isotropic Cu/SAC305/Cu solder interconnects fabricated by high-intensity ultrasound-assisted solidification [J]. Journal of Electronic Materials, 2014, 43: 2467−2478.

[10] REN X L, WANG Y P, ZOU L J, LIU X Y, ZHAO N. Effects of size and cooling rate on solidification behavior of freestanding Sn−3.0Ag−0.5Cu solder balls [J]. Materials Characterization, 2021, 182: 111530.

[11] MUELLER M, WIESE S, ROELLIG M, WOLTER K J. The dependence of composition, cooling rate and size on the solidification behaviour of SnAgCu solders [C]//2007 International Conference on Thermal, Mechanical and Multi-Physics Simulation Experiments in Microelectronics and Micro-Systems. London, UK: IEEE, 2007: 1−10.

[12] MA Z L, SHANG H, DASZKI A A, BELYAKOV S A, GOURLAY C M. Mechanisms of β-Sn nucleation and microstructure evolution in Sn−Ag−Cu solders containing titanium [J]. Journal of Alloys and Compounds, 2019, 777: 1357−1366.

[13] SEO S K, KANG S K, SHIH D Y, LEE H M. An investigation of microstructure and microhardness of Sn−Cu and Sn−Ag solders as functions of alloy composition and cooling rate [J]. Journal of Electronic Materials, 2009, 38: 257−265.

[14] NOBARI A H, MAALEKIAN M, SEELIG K, PEKGULERYUZ M. Effect of Ag, Ni and Bi additions on solderability of lead-free solders [J]. Journal of Electronic Materials, 2017, 46: 4076−4084.

[15] HAMMAD A E. Investigation of microstructure and mechanical properties of novel Sn−0.5Ag−0.7Cu solders containing small amount of Ni [J]. Materials and Design, 2013, 50: 108−116.

[16] VENTURA T, TERZI S, RAPPAZ M, DAHLE A K. Effects of Ni additions, trace elements and solidification kinetics on microstructure formation in Sn−0.7Cu solder [J]. Acta Materialia, 2011, 59: 4197−4206.

[17] WANG H Z, HU X W, JIANG X X. Effects of Ni modified MWCNTs on the microstructural evolution and shear strength of Sn−3.0Ag−0.5Cu composite solder joints [J]. Materials Characterization, 2020, 163: 110287.

[18] LI C J, YAN Y F, GAO T T, XU G D. The microstructure, thermal, and mechanical properties of Sn−3.0Ag−0.5Cu−xSb high-temperature lead-free solder [J]. Materials, 2020, 13: 4443.

[19] RAMLI M I, SALLEH M A A M, IBRAHIM I N A, SAID R M. Effect of Zn additions on thermal and mechanical properties of Sn−0.7Cu−xZn solder alloy [J]. Solid State Phenomena, 2018, 280: 200−205.

[20] ZENG G, MCDONALD S D, GU Q F, TERADA Y, UESUGI, K, YASUDA H, NOGITA K. The influence of Ni and Zn additions on microstructure and phase transformations in Sn−0.7Cu/Cu solder joints [J]. Acta Materialia, 2015, 83: 357−371.

[21] HU X W, LI K, MIN Z X. Microstructure evolution and mechanical properties of $Sn_{0.7}Cu_{0.7}Bi$ lead-free solders produced by directional solidification [J]. Journal of Alloys and Compounds, 2013, 566: 239−245.

[22] WU J, XUE S B, WANG J W, WU M F. Coupling effects of rare-earth Pr and Al_2O_3 nanoparticles on the microstructure and properties of Sn−0.3Ag−0.7Cu low-Ag solder [J]. Journal of Alloys and Compounds, 2019, 784: 471−487.

[23] SEO S K, CHO M G, KANG S K, CHANG J, LEE H M. Minor alloying effects of Ni or Zn on microstructure and micro- hardness of Pb-free solders [C]//2011 IEEE 61st Electronic Components and Technology Conference (ECTC). FL, USA: IEEE, 2011: 84−89.

[24] HAN Y D, GAO Y, ZHANG S T, JING H Y, WEI J, ZHAO L, XU L Y. Study of mechanical properties of Ag nanoparticle-modified graphene/Sn−Ag−Cu solders by nanoindentation [J]. Materials Science and Engineering: A, 2019, 761: 138051.

[25] CHEN X, XUE F, ZHOU J, YAO Y. Effect of In on microstructure, thermodynamic characteristic and mechanical properties of Sn−Bi based lead-free solder [J]. Journal of Alloys and Compounds, 2015, 633: 377−383.

[26] TIAN S, LI S P, ZHOU J, XUE F, CAO R H, WANG F J. Effect of indium addition on interfacial IMC growth and bending properties of eutectic Sn−0.7Cu solder joints [J].

Journal of Materials Science: Materials in Electronics, 2017, 28: 16120−16132.
[27] TIAN S, LI S, ZHOU J, XUE F. Thermodynamic characteristics, microstructure and mechanical properties of Sn−0.7Cu−*x*In lead-free solder alloy [J]. Journal of Alloys and Compounds, 2018, 742: 835−843.
[28] LEE H T, LEE F F, HONG T F, CHEN H W. Effect of in addition on Sn−Ag−Sb lead-free solder system [C]//2008 International Conference on Electronic Materials and Packaging. Taipei: IEEE, 2009: 191−194.
[29] WEI G Q, WANG L. Effects of cooling rate on microstructure and microhardness of lead-free Sn−3.0Ag−0.5Cu solder [C]//2012 13th International Conference on Electronic Packaging Technology & High Density Packaging. Guilin: IEEE, 2013: 453−456.
[30] LEHMAN L P, XING Y Z, BIELER T R, COTTS E J. Cyclic twin nucleation in tin-based solder alloys [J]. Acta Materialia, 2010, 58: 3546−3556.
[31] HAO T, FAN Z Q, ZHAO S X, LUO G N, LIU C S, FANG Q F. Microstructures and properties of ultrafine-grained tungsten produced by equal-channel angular pressing at low temperatures [J]. Journal of Nuclear Materials, 2013, 433(1/2/3): 351−356.
[32] HILLIG W B, TURNBULL D. Theory of crystal growth in undercooled pure liquids [J]. The Journal of Chemical Physics, 1956, 24: 914.
[33] HELFRICH W J, DODD R A. Densities and lattice parameters of tin (indium) solid solutions [J]. Acta Metallurgica, 1964, 12(5): 667−669.
[34] OHNUMA I, MIYASHITA M, LIU X J, OHTANI H, ISHIDA K. Phase equilibria and thermodynamic properties of Sn−Ag based Pb-free solder alloys [J]. IEEE Transactions on Electronics Packaging Manufacturing, 2003, 26: 84−89.
[35] YANG T L, AOKI T, MATSUMOTO K, TORIYAMA K, HORIBE A, MORI H, ORII Y, WU J Y, KAO C R. Full intermetallic joints for chip stacking by using thermal gradient bonding [J]. Acta Materialia, 2016, 113: 90−97.
[36] CHEN Y B, GAO Z Q, LIU Z Q. Temperature gradient induced orientation change of Bi grains in Sn−Bi57−Ag0.7 solder joint [J]. Acta Metallurgica Sinica (English Letters), 2022, 35(7): 1184−1194.
[37] LIN Y F, HAO Y C, OUYANG F Y. Improvement of thermomigration resistance in lead-free Sn3.5Ag alloys by Ag interlayer [J]. Journal of Alloys and Compounds, 2020, 847:156429.

添加 In 对 SAC305 焊料显微组织和性能的影响

任晓磊，王云鹏，赖彦青，史淑艳，刘晓英，邹龙江，赵 宁

大连理工大学 材料科学与工程学院，大连 116024

摘 要：在 Sn−3.0Ag−0.5Cu(SAC305)焊料中熔入 0.5%~10%(质量分数)的 In 粉以改变钎料的显微组织，进而改善焊料的性能。实验结果表明：*β*-Sn(In)、$Ag_3(Sn,In)$和 $Cu_6(Sn,In)_5$ 相存在于所有的含 In 钎料中，在 SAC305−10In 焊料中发现了 $InSn_4$ 物相。随着 In 含量的增加，*β*-Sn 晶粒形核点增加，其形核模型由{101}转变为{301}，从而细化 *β*-Sn 晶粒，使得 *β*-Sn 的形态由粗大晶粒转变为交错晶粒，最后转变为多晶粒。结果表明，这种 *β*-Sn 晶粒形态转变引起细晶强化与固溶强化的联合作用，使得 SAC305−*x*In 焊料的显微硬度随着 In 添加量的增加而显著升高。

关键词：Sn−3.0Ag−0.5Cu；铟；*β*-Sn；过冷度；成核模型；显微硬度

(Edited by Xiang-qun LI)